nature materials

Article

https://doi.org/10.1038/s41563-022-01398-9

Active pixel sensor matrix based on monolayer MoS_2 phototransistor array

Received: 14 November 2021

Accepted: 6 October 2022

Published online: 17 November 2022

Check for updates

Akhil Dodda[1,7], Darsith Jayachandran[1,7], Andrew Pannone[1], Nicholas Trainor[2,3], Sergei P. Stepanoff[2], Megan A. Steves[4], Shiva Subbulakshmi Radhakrishnan[1], Saiphaneendra Bachu[2], Claudio W. Ordonez[4], Jeffrey R. Shallenberger[3], Joan M. Redwing[2,3], Kenneth L. Knappenberger[4], Douglas E. Wolfe[1,2,5] & Saptarshi Das[1,2,3,5,6]

In-sensor processing, which can reduce the energy and hardware burden for many machine vision applications, is currently lacking in state-of-the-art active pixel sensor (APS) technology. Photosensitive and semiconducting two-dimensional (2D) materials can bridge this technology gap by integrating image capture (sense) and image processing (compute) capabilities in a single device. Here, we introduce a 2D APS technology based on a monolayer MoS_2 phototransistor array, where each pixel uses a single programmable phototransistor, leading to a substantial reduction in footprint (900 pixels in ~0.09 cm^2) and energy consumption (100s of fJ per pixel). By exploiting gate-tunable persistent photoconductivity, we achieve a responsivity of ~3.6×10^7 A W^{-1}, specific detectivity of ~5.6×10^{13} Jones, spectral uniformity, a high dynamic range of ~80 dB and in-sensor de-noising capabilities. Further, we demonstrate near-ideal yield and uniformity in photoresponse across the 2D APS array.

Pixel sensors are one of the most ubiquitous and essential types of technologies with a wide range of applications in the era of the Internet of Things (IoT). As the scale and diversity of applications for pixel sensors have grown over time, information conversion and transmission of data through conventional architectures in complementary metal-oxide-semiconductor (CMOS) sensors have become extremely area and energy inefficient[1,2]. Steady progress has been made towards the development of energy-efficient photodetectors through the discovery of new materials, innovation in device engineering and the development of in-sensor or near-sensor computing architectures[3,4]. Due to their atomically thin nature, tunable bandgap and strong light–matter interaction when confined to their monolayer limit, two-dimensional (2D) transition metal dichalcogenides have created tremendous excitement in the optoelectronics community[5–17]. For example, gate-tunable photoconductivity in a WSe_2-based photodiode array has been exploited for image sensing and processing[5]. Similarly, MoS_2 phototransistors have been used as image sensors[6,10], insect-inspired collision detectors[15], watermarks for securing integrated circuits[17] and spike-timing-based photo encoders[16].

Here we introduce a low-power and compact active pixel sensor (APS) technology based on a monolayer MoS_2 phototransistor array that integrates image capture (sense) and image processing (compute) capabilities in a single device. We exploit gate-tunable persistent photoconductivity to achieve high responsivity, high detectivity, spectral uniformity and high dynamic range (HDR), and utilize electrical programmability to achieve fast reset and de-noising capabilities. We also demonstrate 100% yield and uniformity in photoresponse across the 2D APS array. Finally, our 2D APS consumes a miniscule amount of energy (<1 pJ per pixel) and occupies a footprint of <0.09 cm^2 when scaled up to 900 pixels. We believe that the demonstrated 2D APS technology can transform edge sensing in the emerging era of the IoT.

[1]Engineering Science and Mechanics, Penn State University, University Park, PA, USA. [2]Materials Science and Engineering, Penn State University, University Park, PA, USA. [3]Materials Research Institute, Penn State University, University Park, PA, USA. [4]Department of Chemistry, Penn State University, University Park, PA, USA. [5]Applied Research Laboratory, Penn State University, University Park, PA, USA. [6]Electrical Engineering and Computer Science, Penn State University, University Park, PA, USA. [7]These authors contributed equally: Akhil Dodda, Darsith Jayachandran. e-mail: sud70@psu.edu

https://doi.org/10.1038/s41563-022-01398-9

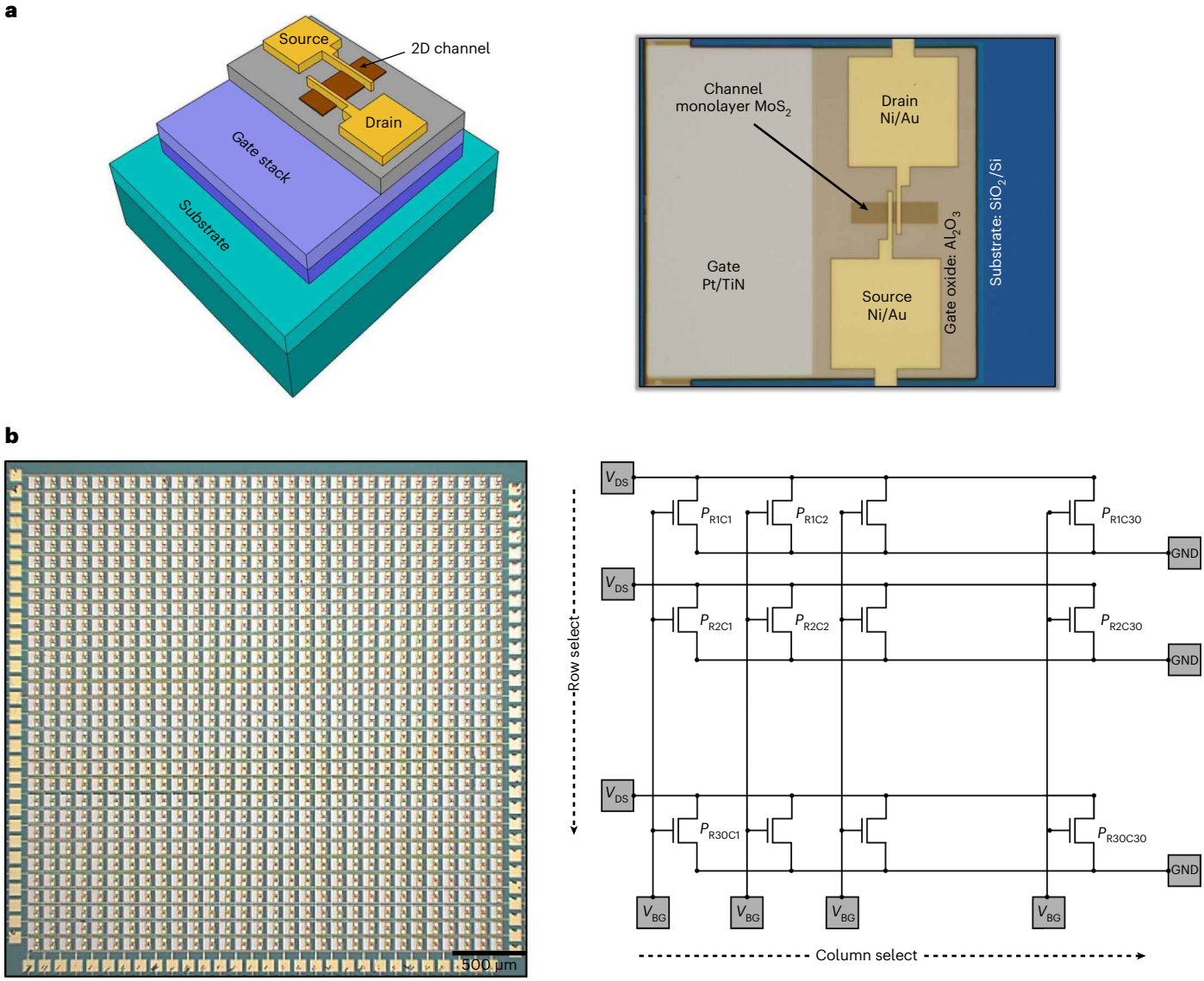

Fig. 1 | 2D APS. a, 3D schematic (left) and optical image (right) of a monolayer MoS_2 phototransistor integrated with a programmable gate stack. The local back-gate stacks, comprising atomic layer deposition grown 50 nm Al_2O_3 on sputter-deposited Pt/TiN, are patterned as islands on top of an Si/SiO_2 substrate. The monolayer MoS_2 used in this study was grown via an MOCVD technique using carbon-free precursors at 900 °C on an epitaxial sapphire substrate to ensure high film quality. Following the growth, the film was transferred onto the TiN/Pt/Al_2O_3 back-gate islands and subsequently patterned, etched and contacted to fabricate phototransistors for the multipixel APS platform. **b**, Optical image of a 900-pixel 2D APS sensor fabricated in a crossbar architecture (left) and the corresponding circuit diagram showing the row and column select lines (right).

2D APS

Figure 1a shows a 3D schematic and an optical micrograph of an individually programmable MoS_2 phototransistor (see Methods for a detailed process flow of monolayer MoS_2 synthesis, film transfer and device fabrication). Figure 1b shows an optical image and associated circuit diagram for a 900-pixel 2D APS matrix in a crossbar architecture with row and column select lines. During exposure, the pixel to be illuminated is selected by applying a back-gate bias (V_{BG}) to the gate pad (to select the column) and a drain bias (V_{DS}) across the source and drain pads (to select the row).

Material characterization of monolayer MoS_2

Figure 2a shows the structure of MoS_2 viewed down its *c* axis with atomic resolution high-angle annular dark-field scanning transmission electron microscopy (HAADF-STEM). The film appears to have a crystalline 2H-MoS_2 structure with very few point defects, which appear as adatoms and vacancies. Figure 2b shows the selected-area electron diffraction (SAED) of MoS_2, which reveals a uniform single-crystalline structure. Figure 2c shows X-ray photoelectron spectroscopy (XPS) of the core-level spectrum of Mo 3*d*, exhibiting two peaks at 229.17 eV and 232.32 eV corresponding to MoS_2 Mo^{4+} $3d_{5/2}$ and Mo^{4+} $3d_{3/2}$, respectively[18]. In addition to the molybdenum peaks, Fig. 2d shows the sulfur peaks corresponding to the doublet of S^{2-} $2p_{3/2}$ and S^{2-} $2p_{1/2}$, which further confirm the 2H-MoS_2 crystal structure[19,20]. The calculated atomic ratio between S^{2-} 2*p* and Mo^{4+} 3*d* is ~2.08, indicating sulfur-rich MoS_2 with good crystallinity[7].

Figure 2e,f, respectively, shows the Raman spectra and corresponding spatial colourmaps of the peak separation between the two Raman active modes, E^1_{2g} and A_{1g}, measured over a 40 µm × 40 µm area for the as-grown MoS_2 film; Fig. 2g,h, respectively, shows the photoluminescence (PL) spectra and corresponding spatial colourmaps of the PL peak position measured over the same area (see Extended Data Fig. 1a–d for similar results on the post-transfer film). These results confirm uniformity in the as-grown and post-transfer films. Extended

https://doi.org/10.1038/s41563-022-01398-9

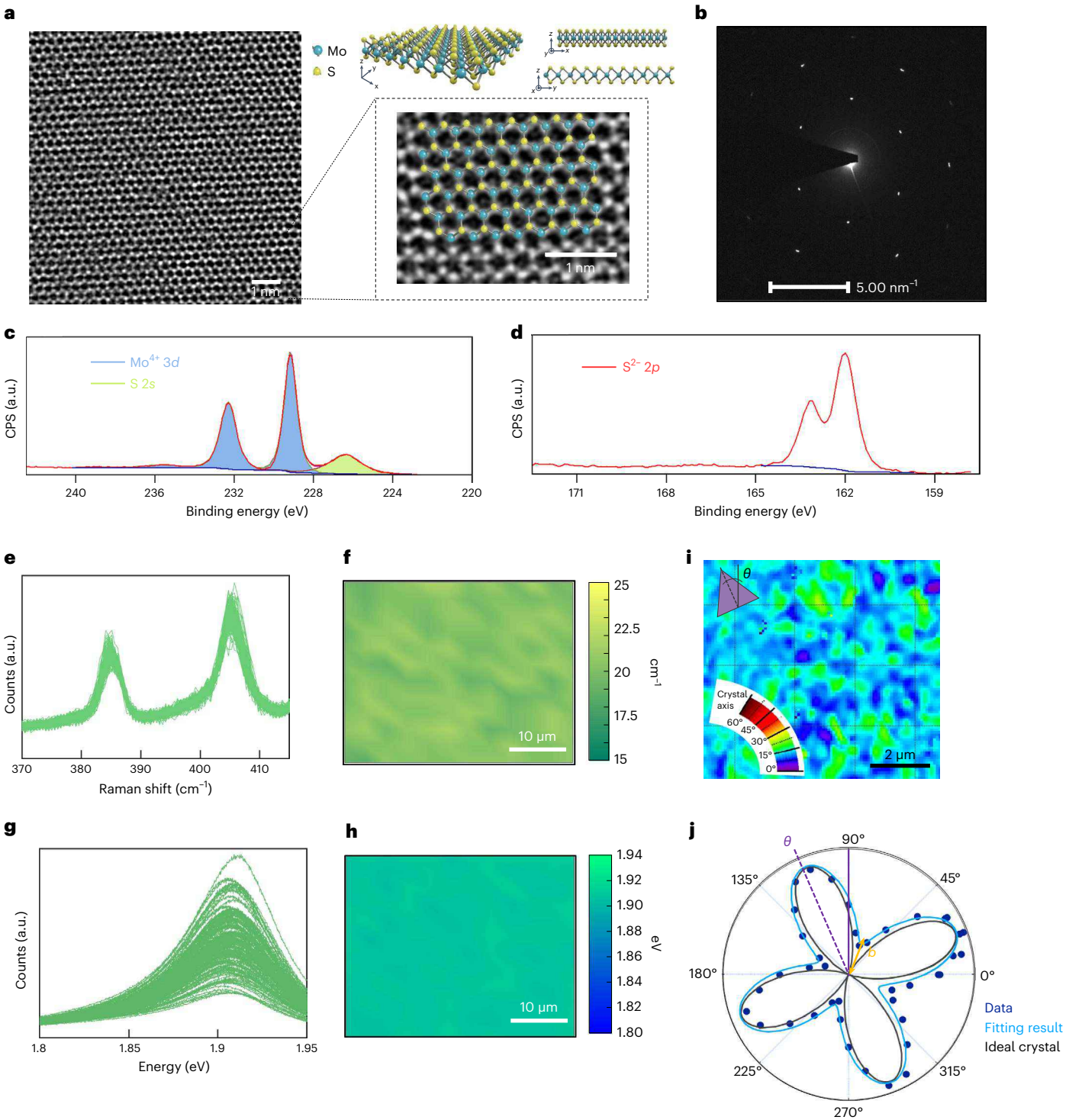

Fig. 2 | Characterization of monolayer MoS_2. a, Structure of MoS_2 viewed down its *c* axis with atomic-resolution HAADF-STEM imaging at an accelerating voltage of 80 kV. Inset: the atomic model of 2H-MoS_2 overlayed on the STEM image. **b**, SAED of the monolayer MoS_2, which reveals a uniform single-crystalline structure. **c**,**d**, XPS of Mo 3*d* (**c**) and S 2*p* (**d**) core levels of monolayer MoS_2 film. **e**,**f**, Raman spectra (**e**) and corresponding spatial colourmap of peak separation between the two Raman active modes, E^1_{2g} and A_{1g}, measured over a 40 μm × 40 μm area, for as-grown MoS_2 film (**f**). **g**,**h**, PL spectra (**g**) and corresponding spatial colourmap of the PL peak position (**h**), measured over the same area as in **f**. The mean peak separation was found to be ~20.2 cm^{-1} with a standard deviation of ~0.6 cm^{-1} and the mean PL peak position was found to be at ~1.91 eV with a standard deviation of ~0.002 eV. **i**, Map of the relative crystal orientation of the MoS_2 film obtained by fitting the polarization-dependence of the SHG response shown in **j**, which is an example polarization pattern obtained from a single pixel of **i** by rotating the fundamental polarization and collecting the harmonic signal at a fixed polarization.

Data Fig. 1e,f, respectively, shows the bar plots for the mean peak separation between E^1_{2g} and A_{1g} and the mean PL peak position, along with their corresponding standard deviation values for the as-grown and post-transfer films in all five locations. The difference in mean PL peak position between the as-grown and post-transfer films is noticeable and can be attributed to the strain in the film introduced during the synthesis, which gets partially relieved during the transfer process[21]. This difference in strain between the as-grown and post-transfer films

is further confirmed by performing polarization-resolved second-harmonic generation (SHG) measurements.

Polarization-resolved SHG offers a rapid, non-destructive approach to determining the structural properties of 2D materials through analysis of the second-order nonlinear susceptibility tensor ($\chi^{(2)}$) (refs. [22–25]). Analysis of the crystal orientation of the as-grown film indicates that the film consists of mostly a single-crystal orientation of ~15° with respect to the laboratory frame, with a standard deviation of 2.5°. This is expected for a TMD film grown on an epitaxial substrate, which promotes the growth of unidirectional crystals[26]. However, fitting the polarization-resolved SHG data shown in Fig. 2i required the incorporation of a parameter to account for isotropic contributions to the four-fold polar pattern expected for a single-defect-free MoS_2 crystal shown in Fig. 2j. The necessity of this parameter to obtain an accurate fit to the experimental data suggests that the sample exhibits inhomogeneous crystal orientations or defects occurring below the spatial resolution of the optical measurement (~160 nm). Supplementary Information 1 shows the presence of strain in both as-grown and post-transfer MoS_2 films by collecting the SHG signal at all harmonic angles while the polarization plane of the fundamental was varied, that is, without an analyser in the detection path. Finally, the surface morphology and thickness of the as-grown and post-transferred films were characterized using atomic force microscopy (AFM) as shown in Extended Data Fig. 2a,b.

Electrical characterization of monolayer MoS_2 phototransistor

Figure 3a shows the transfer characteristics, that is, the source-to-drain current (I_{DS}) as a function of the local back-gate voltage (V_{BG}), at a source-to-drain voltage (V_{DS}) of 1 V and measured in the dark for 720 MoS_2 phototransistors (80% of the devices that constitute the 2D APS array) with channel lengths (L) of 1 µm and channel widths (W) of 5 µm. Figure 3b–e, respectively, shows the distribution of electron field-effect mobility values (μ_{FE}) extracted from the peak transconductance, current on/off ratios ($r_{ON/OFF}$), subthreshold slopes (SS) over three orders of magnitude change in I_{DS} and threshold voltages (V_{TH}) extracted at an isocurrent of 500 nA µm for these 720 MoS_2 phototransistors. The mean values for μ_{FE}, $r_{ON/OFF}$, SS and V_{TH} were found to be ~23.6 $cm^2\,V^{-1}\,s^{-1}$, 6.4×10^7, 485 mV per decade and 2.54 V, respectively, with corresponding standard deviation values of 7 $cm^2\,V^{-1}\,s^{-1}$, 8.2×10^6, 115 mV per decade and 0.57 V, respectively. Our μ_{FE}, $r_{ON/OFF}$, SS and V_{TH} values and the corresponding device-to-device variations are on par with the state-of-the-art literature on large-area-grown MoS_2. Extended Data Fig. 3 shows minimal gate hysteresis in the transfer characteristics of 49 representative MoS_2 phototransistors when measured in air.

We also investigated the pixel-to-pixel variation in the photoresponse of the 2D APS platform. Figure 3f shows the pre- and post-illumination transfer characteristics of 720 phototransistors after exposure to white light with an illumination intensity (P_{in}) of 20 W m^{-2} for an exposure time (τ_{exp}) of 1 s while the back-gate bias (V_{exp}) is held at −1 V. Figure 3g–j, respectively, shows the corresponding histograms of the distribution of dark (I_{DARK}) and photocurrent (I_{PH}), the ratio of post-illumination photocurrent to dark current (r_{PH}), responsivity (R) and detectivity (D^*), each measured at $V_{BG} = -1$ V. The mean values for I_{DARK}, I_{PH}, r_{PH}, R and D^* were found to be $\sim 2.9 \times 10^{-11}$ A µm^{-1}, $\sim 1.84 \times 10^{-7}$ A µm^{-1}, $\sim 1.84 \times 10^5$, $\sim 1.84 \times 10^3$ A W^{-1} and $\sim 8.7 \times 10^9$ Jones, respectively, with corresponding standard deviation values of $\sim 1.7 \times 10^{-10}$ A µm^{-2}, $\sim 1.9 \times 10^{-7}$ A µm^{-1}, $\sim 1.9 \times 10^5$, $\sim 2 \times 10^3$ A W^{-1} and $\sim 9.1 \times 10^9$ Jones, respectively.

Mechanism of photoresponse in monolayer MoS_2 phototransistor

Next, we elucidate the photoresponse mechanism and demonstrate some of the key features of our monolayer-MoS_2-based 2D APS technology. Supplementary Information 2 shows the post-illumination transfer characteristics of a representative phototransistor measured using $V_{DS} = 1$ V in the dark after $\tau_{exp} = 1$ s exposure to different P_{in} spanning ~4 orders of magnitude for red, green and blue wavelengths, respectively. During the exposures to the light-emitting diodes, the phototransistor was biased in the on-state (top panel) and off-state (bottom panel) by applying $V_{exp} = 2$ V and −2 V, respectively, to the local back-gate. When the phototransistor was exposed in the on-state, there are little-to-no changes in the post-illumination device characteristics. This is because photocarriers generated in the semiconducting 2D channel drift towards the respective electrodes under the applied $V_{DS} = 1$ V, resulting in non-persistent photoconductivity beyond optical illumination. However, for illuminations in the off-state, noticeable shifts are observed in the threshold voltage (V_{TH}) of the device post-illumination. This can be ascribed to the phenomenon of gate-tunable photocarrier trapping, that is, the photogating effect.

Many factors can influence photogenerated carrier trapping in monolayer MoS_2 phototransistors. According to previous studies based on exfoliated and large-area-grown MoS_2, carrier trapping can occur in the band tail states in the conduction and valence bands of MoS_2; these states can originate from structural defects such as vacancies, grain boundaries, dislocations and strain in the MoS_2 film, or localized trap states at and/or near the MoS_2/dielectric interface stemming from defects in the gate dielectric, from water and other gaseous adsorbates from an ambient environment, or residue from the device fabrication[5,7,9,11,27–38]. While we cannot rule out carrier trapping in the band tail states in the conduction and valence bands of MoS_2, given the relatively high quality of the MoS_2 film revealed through high-resolution transmission electron microscopy and XPS and the relatively damage-free transfer and clean fabrication processes revealed through Raman and PL maps, and the low device-to-device variation, we believe that most of the carrier trapping occurs in the border traps located in the dielectric at and/or near the dielectric/channel interface. This can be substantiated by performing bias-temperature instability (BTI) tests originally developed to study interface traps in conventional silicon transistors (see Supplementary Information 3 for the BTI study of MoS_2 phototransistors). Irrespective of the illumination conditions and bias temperature, the V_{TH} of the MoS_2 phototransistor shifts towards a more negative voltage with increasing t_{stress}, confirming the presence of hole-capturing border traps in the oxide. Furthermore, relatively large changes in ΔV_{TH} at higher temperatures reaffirm the creation of more trap states in the oxide. Finally, under illumination, more photogenerated holes are available for capture, which leads to greater shifts in V_{TH}.

Without any electrical intervention the de-trapping process can be rather slow, leading to persistent change in V_{TH}. Figure 4a–c shows the post-illumination persistent photocurrent (I_{ph}) read out with $V_{BG} = 0$ V and $V_{DS} = 1$ V as a function of P_{in} for different τ_{exp} at red, green and blue wavelengths, respectively (see Extended Data Fig. 4 for the corresponding post-illumination transfer characteristics). Note that $V_{exp} = -2$ V for all cases. As expected, I_{ph} increases monotonically with P_{in} and τ_{exp}. This phenomenon is equivalent to charge integration by the photodiode in a CMOS-based APS technology. However, for our 2D APS technology, the stored charge naturally translates into the abovementioned V_{TH} shift, which can be read out as I_{ph}, thus eliminating the need for an additional transistor that converts the charge to read out voltage/current as in CMOS-based APSs. Note that the dynamic range of our 2D APS is ~80 dB for all three wavelengths investigated. Supplementary Video 1 shows the HDR image transcription for different wavelengths of light. The blue and green Ts are captured in less than 3 s, whereas transcription of the red T requires a longer exposure of ~10 s. This can be ascribed to the spectral non-uniformity of the photosensing material and is a commonly encountered problem in the development of image sensors.

For CMOS-based APSs, spectral non-uniformity in the photoresponse is circumvented through additional exposure control and amplifier circuitry to allow enough charge accumulation and

https://doi.org/10.1038/s41563-022-01398-9

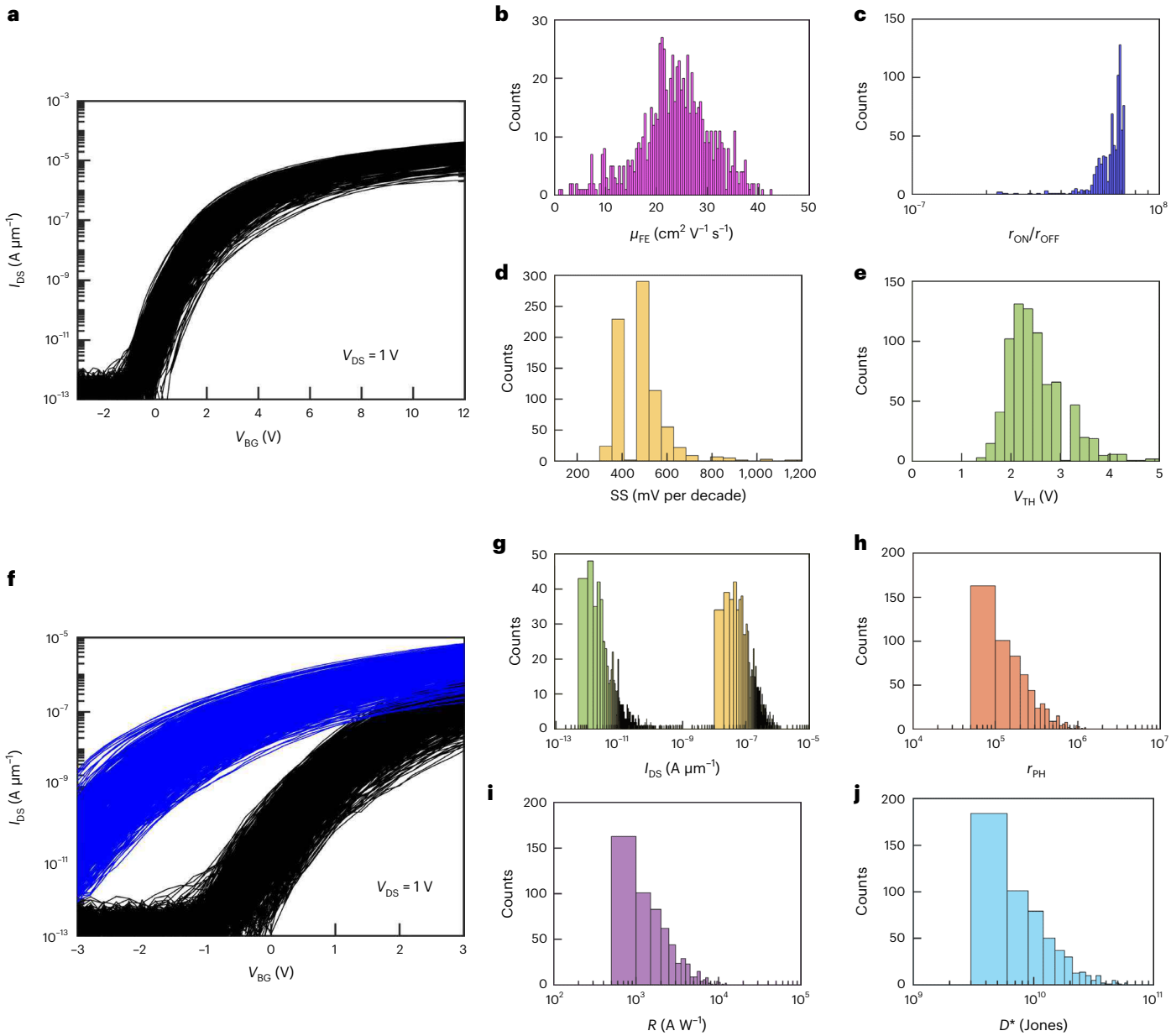

Fig. 3 | Device-to-device variation in the characteristics of MoS_2 phototransistors. a, Transfer characteristics, that is, source to drain current (I_{DS}) as a function of the local back-gate voltage (V_{BG}), at a source-to-drain voltage (V_{DS}) of 1 V and measured in the dark for 720 monolayer MoS_2 phototransistors (80% of the devices that constitute the vision array) with channel lengths (L) of 1 μm and channel widths (W) of 5 μm. **b**–**d**, Device-to-device variation is represented using histograms of electron field-effect mobility values (μ_{FE}) extracted from the peak transconductance (**b**), current on/off ratios ($r_{ON/OFF}$) (**c**), subthreshold slopes (SS) over three orders of magnitude change in I_{DS} (**d**) and threshold voltages (V_{TH}) extracted at an isocurrent of 500 nA μm^{-1} for 80% of devices in the 2D APS array (**e**). **f**, Pre- and post-illumination transfer characteristics of 720 monolayer MoS_2 phototransistors after exposure to white light with P_{in} = 20 W m^{-2} at V_{exp} = −3 V for τ_{exp} = 1 s. **g**–**j**, Histograms of dark current (I_{DARK}) (green) and photocurrent (I_{PH}) (yellow) (**g**), the ratio of post-illumination photocurrent to dark current (r_{PH}) (**h**), responsivity (R) (**i**) and detectivity (D^*) (**j**), all measured at V_{BG} = −1 V.

conversion of charge to measure voltage/current, respectively, both of which add area and energy overhead. In contrast, our 2D APS technology eliminates the need for extensive peripherals by exploiting a gate-tunable persistent photocurrent. Figure 4d–f, respectively, shows I_{PH} read out with V_{BG} = 0 V and V_{DS} = 1 V as a function of P_{in} for different V_{exp} and τ_{exp} = 100 ms at red, green and blue wavelengths, respectively (see Extended Data Fig. 5 for the corresponding post-illumination transfer characteristics). Note that $I_{PH} \approx 100$ pA for P_{in} = 15 W m^{-2} is achieved with V_{exp} = −4, −2, −3 V at red, green and blue illuminations, respectively, for the same τ_{exp} = 100 ms. This clearly shows that our 2D APS technology can achieve spectral uniformity without adding area and energy overhead. We have also extended our measurements to high frequencies and measured the response of the MoS_2 phototransistor using τ_{exp} = 100 ns. Extended Data Fig. 6 shows the pre- and post-illumination transfer characteristics of a representative MoS_2 phototransistor after being exposed to blue illumination with an intensity of P_{in} = 15 W m^{-2} at V_{exp} = −4 V for t_{exp} = 100 ns. We observe a change in the post-illumination transfer characteristics, indicating that the charge trapping in the MoS_2 phototransistor can occur as rapidly as 100 ns.

Photodetection metrics

Overall, our 2D APS platform offers the capability to dynamically reconfigure the responsivity ($R = I_{ph}/WLP_{in}$) by adjusting V_{exp} without tuning τ_{exp}. Figure 5a–c shows R as a function of V_{exp} and P_{in} for τ_{exp} = 10 s at red,

https://doi.org/10.1038/s41563-022-01398-9

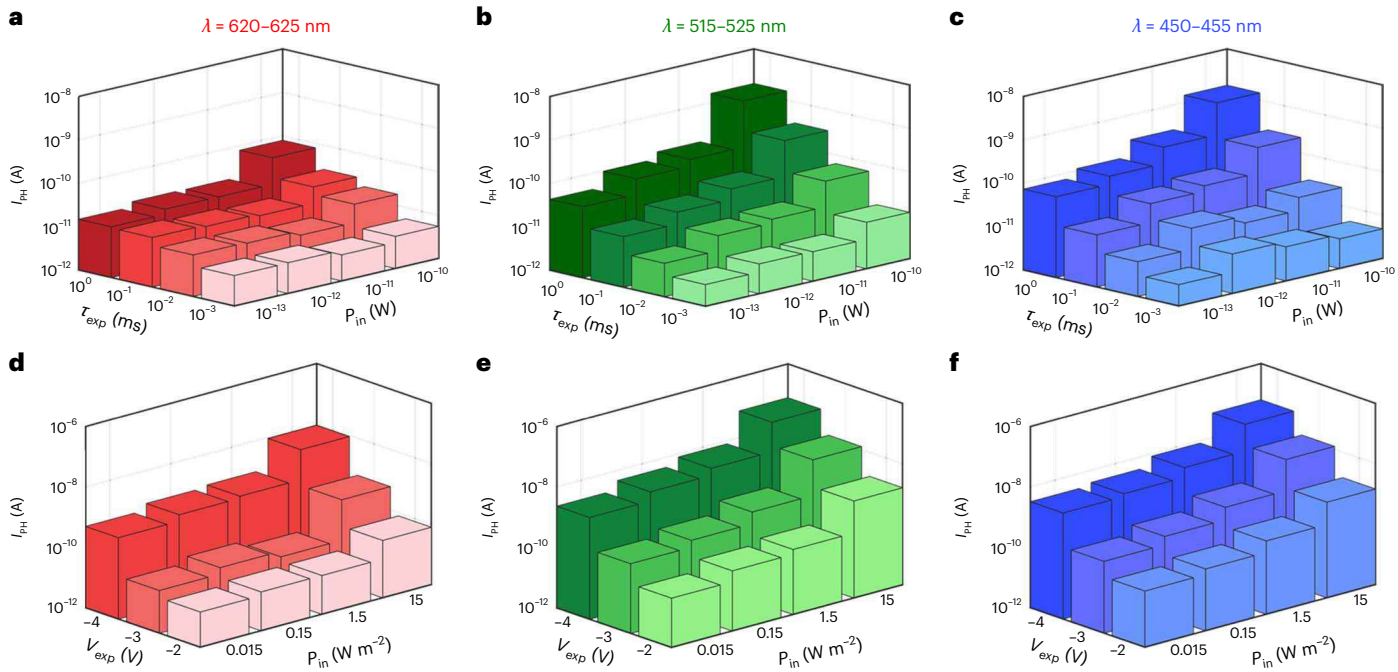

Fig. 4 | HDR and spectral uniformity. a–**c**, The post-illumination persistent photocurrent (I_{PH}) read out using $V_{BG} = 0$ V and $V_{DS} = 1$ V under different exposure times (τ_{exp}) is plotted against P_{in} for $V_{exp} = -2$ V at red (**a**), green (**b**) and blue (**c**) wavelengths. Clearly, the 2D APS demonstrates HDR for all wavelengths investigated. **d**–**f**, However, the 2D APS displays spectral non-uniformity in the photoresponse, which can be adjusted by exploiting gate-tunable persistent photoconductivity, that is, by varying V_{exp}. This is shown by plotting I_{PH} against P_{in} for different V_{exp} at red (**d**), green (**e**) and blue (**f**) wavelengths.

green and blue wavelengths, respectively. R increases monotonically with V_{exp}. While the R values are comparable to those in earlier reports on MoS_2 (refs. [39,40]), the magnitude of R can be further increased by using more negative V_{exp} and longer t_{exp}, and by using more positive V_{BG} and larger V_{DS} for read out of I_{ph}. Figure 5d shows the pre- and post-illumination transfer characteristics after exposure to blue illumination at $V_{exp} = -6$ V for $t_{exp} = 200$ s with $V_{DS} = 5$ V. Figure 5e shows that the magnitude of R can reach very high values of as much as $\sim 3.6 \times 10^7$ A W^{-1} when extracted at $V_{BG} = 5$ V. However, note that the noise current (I_{noise}), in units of A Hz$^{-1/2}$, extracted from the dark current, is high under the aforementioned biasing conditions. Therefore, a better benchmarking metric for the MoS_2 phototransistor is the specific detectivity (D^*), which is defined as $D^* = \sqrt{A}/\mathrm{NEP}$, where $A = WL$ is the area of the phototransistor and NEP is the noise equivalent power given by $\mathrm{NEP} = I_{noise}/R$. Figure 5f shows D^*, which expectedly follows a non-monotonic trend with V_{BG}; the peak D^* reaches a very high value of $\sim 5.6 \times 10^{13}$ Jones. See Supplementary Information 4 for a benchmarking table comparing our MoS_2 phototransistor with other 2D photodetectors. Finally, the energy expenditure for image transcription can be calculated from equation (1).

$$E = \frac{1}{2} C_G V_{exp}^2 + V_{DS} \int_0^{\tau_{exp}} I_{DS}(t)\, dt \quad (1)$$

Here, I_{DS} is the source-to-drain current in the MoS_2 phototransistor during illumination at $V_{BG} = V_{exp}$ and $C_G = \varepsilon_0 \varepsilon_{ox} WL/t_{ox}$ is the gate capacitance; $\varepsilon_0 = 8.85 \times 10^{-12}$ F m^{-1} is the vacuum permittivity, $\varepsilon_{OX} = 10$ and $t_{OX} = 50$ nm are, respectively, the relative permittivity and thickness of Al_2O_3, and W and L are the channel width and length of the MoS_2 phototransistor. The first term in equation (1) represents the energy spent to charge the gate capacitor to V_{exp} and the second term represents the energy dissipation in the phototransistor due to the flow of I_{DS}, that is, the sum of the dark current and photocurrent, during the entire duration of illumination (τ_{exp}). Figure 5g shows E as a function of V_{exp}. E was found to be <200 fJ even for the most negative V_{exp}.

Reset and de-noising

While the photogating effect allows our 2D APS technology to achieve HDR and spectral uniformity, the retention of optical information in the form of trapped charges is detrimental to video streaming applications. To accelerate the de-trapping process, large positive reset voltage (V_{reset}) pulses can be applied to the local back-gate of the post-illumination MoS_2 phototransistor.

Figure 6a shows the post-reset transfer characteristics of a representative MoS_2 phototransistor with $V_{reset} = 12$ V applied for $t_{reset} = 100$ µs. During reset, the source and drain terminals are kept grounded, that is, $V_{DS} = 0$ V. Note that the post-illumination to post-reset conductance ratio (CR) can be adjusted by changing the magnitude of V_{reset}, as shown in Fig. 6b. In other words, a fast refresh can be achieved irrespective of the illumination level. Brighter illumination invokes higher conductance change and hence requires higher V_{reset}, which leads to higher energy expenditure ($E_{reset} = \frac{1}{2} C_G V_{reset}^2$) as shown in Fig. 6c. Interestingly, even for the highest $V_{reset} = 12$ V, E_{reset} is ~0.6 pJ.

Next, we elucidate the de-noising capability of our 2D APS technology. Note that CMOS-based APS technology adopts extensive peripheral circuitry to implement sophisticated de-noising algorithms, which adds area and energy overhead. Figure 6d and Supplementary Video 2 show the colourmaps of the time evolution of conductance (G) measured at $V_{BG} = 0$ V while capturing an image of the letter T in the presence of background noise with and without V_{reset}. To generate the noisy images, the input current to the light-emitting diode corresponding to each pixel was superimposed with a zero mean white Gaussian random noise of standard deviation $\sigma_I = 2$ mA. This translates into a fluctuation in P_{in} with a standard deviation of $\sigma_P = 0.6$ W m^{-2} for each pixel. In the absence of reset ($V_{reset} = 0$ V), the pixel sensors which are expected to remain in the low conductance state also get randomly photoexcited due to noise, making it impossible to capture the pattern present in the image. In contrast, when reset is enabled ($V_{reset} = 8$ V), the random photoexcitations in the unintended phototransistors are compensated, allowing the 2D APS matrix to accurately capture the letter T under noisy illumination. This demonstration highlights the

https://doi.org/10.1038/s41563-022-01398-9

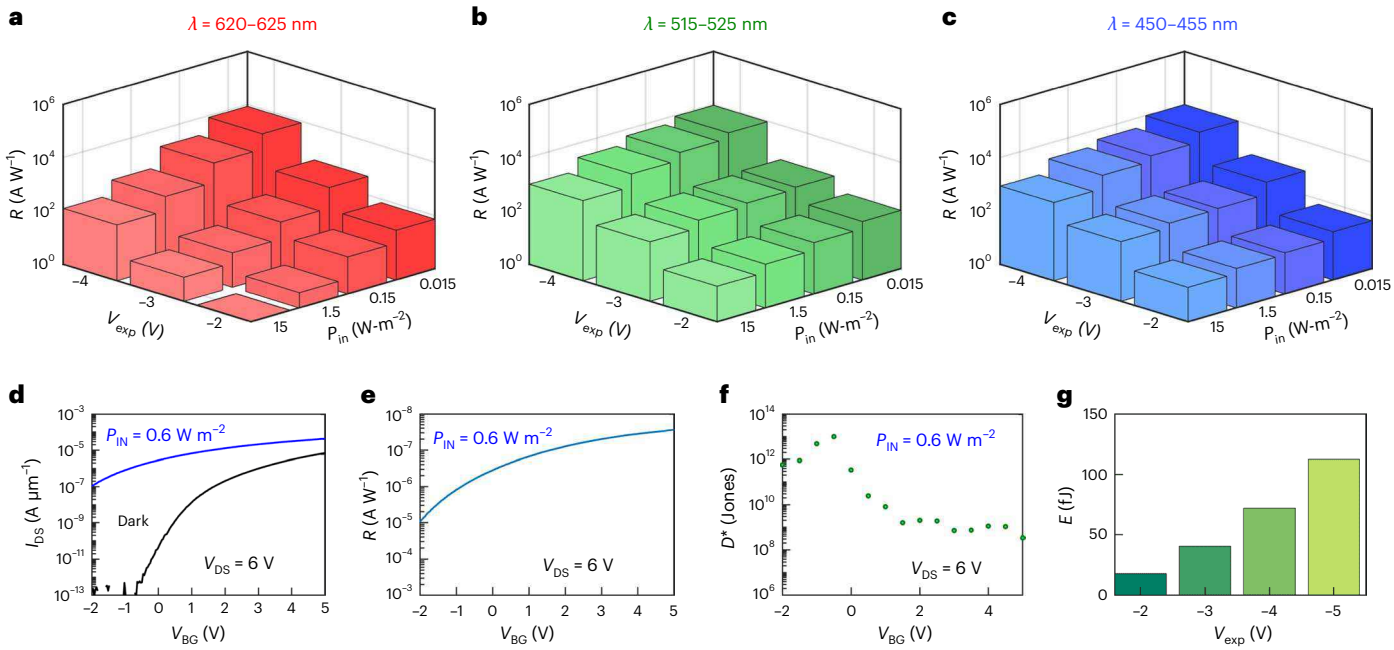

Fig. 5 | Photodetection metrics. a–**c**, Responsivity (R) as a function of V_{exp} and P_{in} for τ_{exp} = 100 ms for red (**a**), green (**b**) and blue (**c**) wavelengths. R increases monotonically with the magnitude of V_{exp}. **d**, Transfer characteristics of a representative 2D APS in the dark and post-illumination at V_{exp} = −6 V with P_{in} = 0.6 W m^{-2} for τ_{exp} = 200 s and V_{DS} = 6 V. **e**, R as a function of V_{BG}. For V_{DS} = 6 V and V_{BG} = 5 V we extract an R value of ~3.6 × 10^7 A W^{-1}. **f**, Specific detectivity (D^*) as a function of V_{BG} at different V_{DS}. At lower V_{BG}, both R and I_{noise}, that is, the dark current obtained from **d**, are low, leading to lower D^*, whereas at higher V_{BG} both R and I_{noise} are high, also leading to lower D^*. Peak D^* can reach as high as ~5.6 × 10^{13} Jones. **g**, Energy consumption per pixel (E) as a function of V_{exp}.

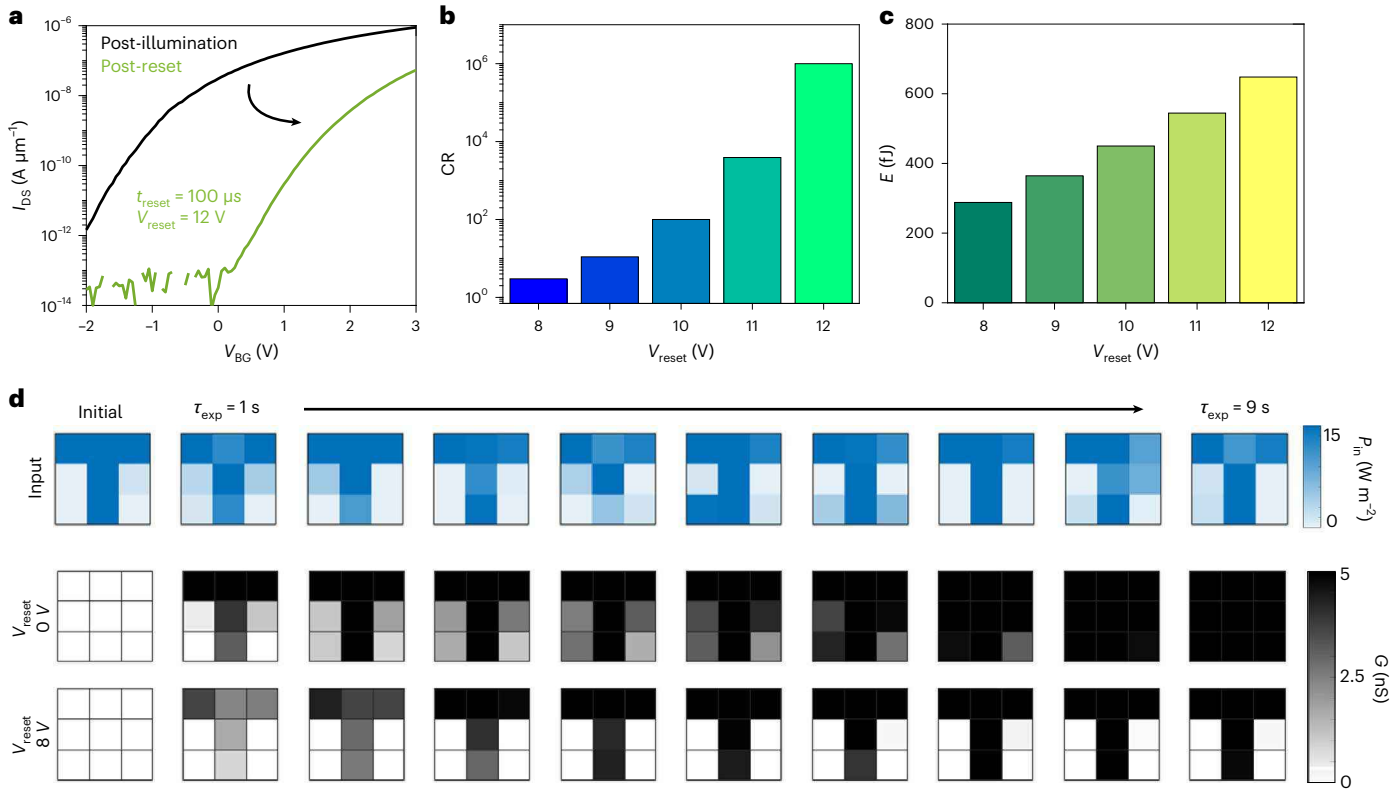

Fig. 6 | Fast reset and de-noising. a, After the read out, each pixel can be reset by applying a reset voltage (V_{reset}) for time periods as low as t_{reset} = 100 μs. **b**, The conductance ratio (CR), defined as the ratio between the conductance values before and after the application of a reset voltage, is plotted against different V_{reset}. **c**, Energy expenditure for reset operations under different V_{reset}. **d**, Heatmaps of conductance (G) measured at V_{BG} = 0 V from the image sensor with and without V_{reset} when exposed to images under noisy conditions. Clearly, application of V_{reset} helps in de-noising image acquisition.

importance of in-sensor compute capability in perceiving information obscured by noise.

In summary, we have demonstrated a monolayer MoS_2 phototransistor-based multipixel APS technology that operates with a miniscule energy budget, occupies a small device footprint, and combines sensing and compute to achieve HDR, spectral uniformity, reconfigurable photoresponsivity, fast reset and de-noising capabilities. Our 2D APS technology can benefit resource-limited edge devices in the rapidly growing IoT era.

Online content

Any methods, additional references, Nature Research reporting summaries, source data, extended data, supplementary information, acknowledgements, peer review information; details of author contributions and competing interests; and statements of data and code availability are available at https://doi.org/10.1038/s41563-022-01398-9.

References

1. Mendis, S., Kemeny, S. E. & Fossum, E. R. CMOS active pixel image sensor. *IEEE Trans. Electron Devices* **41**, 452–453 (1994).
2. Mendis, S. K. et al. CMOS active pixel image sensors for highly integrated imaging systems. *IEEE J. Solid-State Circuits* **32**, 187–197 (1997).
3. Zhou, F. & Chai, Y. Near-sensor and in-sensor computing. *Nat. Electron.* **3**, 664–671 (2020).
4. Dodda, A., Trainor, N., Redwing, J. & Das, S. All-in-one, bio-inspired, and low-power crypto engines for near-sensor security based on two-dimensional memtransistors. *Nat. Commun.* **13**, 1–12 (2022).
5. Mennel, L. et al. Ultrafast machine vision with 2D material neural network image sensors. *Nature* **579**, 62–66 (2020).
6. Ma, S. et al. A 619-pixel machine vision enhancement chip based on two-dimensional semiconductors. *Sci. Adv.* **8**, eabn9328 (2022).
7. Hong, S. et al. Highly sensitive active pixel image sensor array driven by large-area bilayer MoS_2 transistor circuitry. *Nat. Commun.* **12**, 1–11 (2021).
8. Nur, R. et al. High responsivity in MoS_2 phototransistors based on charge trapping HfO_2 dielectrics. *Commun. Mater.* **1**, 1–9 (2020).
9. Seo, S. et al. Artificial optic-neural synapse for colored and color-mixed pattern recognition. *Nat. Commun.* **9**, 5106 (2018).
10. Choi, C. et al. Curved neuromorphic image sensor array using a MoS_2-organic heterostructure inspired by the human visual recognition system. *Nat. Commun.* **11**, 1–9 (2020).
11. Wang, C.-Y. et al. Gate-tunable van der Waals heterostructure for reconfigurable neural network vision sensor. *Sci. Adv.* **6**, eaba6173 (2020).
12. Hong, S. et al. Sensory adaptation and neuromorphic phototransistors based on $CsPb(Br_{1-x}I_x)_3$ perovskite and MoS_2 hybrid structure. *ACS Nano* **14**, 9796–9806 (2020).
13. Hou, Y.-X. et al. Large-scale and flexible optical synapses for neuromorphic computing and integrated visible information sensing memory processing. *ACS Nano* **15**, 1497–1508 (2020).
14. Hong, S. et al. Neuromorphic active pixel image sensor array for visual memory. *ACS Nano* **15**, 15362–15370 (2021).
15. Jayachandran, D. et al. A low-power biomimetic collision detector based on an in-memory molybdenum disulfide photodetector. *Nat. Electron.* **3**, 646–655 (2020).
16. Radhakrishnan, S. S. et al. A sparse and spike-timing-based adaptive photo encoder for augmenting machine vision for spiking neural networks. *Adv. Mater.* https://doi.org/10.1002/adma.202202535 (2022).
17. Oberoi, A., Dodda, A., Liu, H., Terrones, M. & Das, S. Secure electronics enabled by atomically thin and photosensitive two-dimensional memtransistors. *ACS Nano* **15**, 19815–19827 (2021).
18. Kondekar, N. P., Boebinger, M. G., Woods, E. V. & McDowell, M. T. In situ XPS investigation of transformations at crystallographically oriented MoS_2 interfaces. *ACS Appl. Mater. Interfaces* **9**, 32394–32404 (2017).
19. Syari'ati, A. et al. Photoemission spectroscopy study of structural defects in molybdenum disulfide (MoS_2) grown by chemical vapor deposition (CVD). *Chem. Commun.* **55**, 10384–10387 (2019).
20. Fominski, V. et al. Reactive pulsed laser deposition of clustered-type MoS_x (x ~ 2, 3, and 4) films and their solid lubricant properties at low temperature. *Nanomaterials* **10**, 653 (2020).
21. Schauble, K. et al. Uncovering the effects of metal contacts on monolayer MoS_2. *ACS Nano* **14**, 14798–14808 (2020).
22. Li, Y. et al. Probing symmetry properties of few-layer MoS_2 and h-BN by optical second-harmonic generation. *Nano Lett.* **13**, 3329–3333 (2013).
23. Mennel, L. et al. Optical imaging of strain in two-dimensional crystals. *Nat. Commun.* **9**, 1–6 (2018).
24. Steves, M. A. et al. Unexpected near-infrared to visible nonlinear optical properties from 2-D polar metals. *Nano Lett.* **20**, 8312–8318 (2020).
25. Psilodimitrakopoulos, S. et al. Ultrahigh-resolution nonlinear optical imaging of the armchair orientation in 2D transition metal dichalcogenides. *Light Sci. Appl.* **7**, 18005–18005 (2018).
26. Chubarov, M. et al. Wafer-scale epitaxial growth of unidirectional WS_2 monolayers on sapphire. *ACS Nano* **15**, 2532–2541 (2021).
27. Schranghamer, T. F., Sharma, M., Singh, R. & Das, S. Review and comparison of layer transfer methods for two-dimensional materials for emerging applications. *Chem. Soc. Rev.* https://doi.org/10.1039/D1CS00706H (2021).
28. Furchi, M. M., Polyushkin, D. K., Pospischil, A. & Mueller, T. Mechanisms of photoconductivity in atomically thin MoS_2. *Nano Lett.* **14**, 6165–6170 (2014).
29. Fang, H. & Hu, W. Photogating in low dimensional photodetectors. *Adv. Sci.* **4**, 1700323 (2017).
30. Peng, B. et al. Achieving ultrafast hole transfer at the monolayer MoS_2 and $CH_3NH_3PbI_3$ perovskite interface by defect engineering. *ACS Nano* **10**, 6383–6391 (2016).
31. Chen, M. et al. Multibit data storage states formed in plasma-treated MoS_2 transistors. *ACS Nano* **8**, 4023–4032 (2014).
32. Zhu, W. et al. Electronic transport and device prospects of monolayer molybdenum disulphide grown by chemical vapour deposition. *Nat. Commun.* **5**, 1–8 (2014).
33. Ghatak, S., Pal, A. N. & Ghosh, A. Nature of electronic states in atomically thin MoS_2 field-effect transistors. *ACS Nano* **5**, 7707–7712 (2011).
34. Liao, F. et al. Bioinspired in-sensor visual adaptation for accurate perception. *Nat. Electron.* **5**, 84–91 (2022).
35. Late, D. J., Liu, B., Matte, H. S. S. R., Dravid, V. P. & Rao, C. N. R. Hysteresis in single-layer MoS_2 field effect transistors. *ACS Nano* **6**, 5635–5641 (2012).
36. Jang, H. et al. An atomically thin optoelectronic machine vision processor. *Adv. Mater.* **32**, e2002431 (2020).
37. Choi, C. et al. Curved neuromorphic image sensor array using a MoS_2–organic heterostructure inspired by the human visual recognition system. *Nat. Commun.* **11**, 5934 (2020).
38. Arnold, A. J. et al. Mimicking neurotransmitter release in chemical synapses via hysteresis engineering in MoS_2 transistors. *ACS Nano* **11**, 3110–3118 (2017).
39. Lopez-Sanchez, O., Lembke, D., Kayci, M., Radenovic, A. & Kis, A. Ultrasensitive photodetectors based on monolayer MoS_2. *Nat. Nanotechnol.* **8**, 497–501 (2013).
40. Zhang, W. et al. High-gain phototransistors based on a CVD MoS_2 monolayer. *Adv. Mater.* **25**, 3456–3461 (2013).

Methods

Fabrication of local back-gate islands

To define the back-gate island regions, a commercially bought substrate (285 nm SiO_2 on p^{++}-Si) was spin-coated with bilayer photoresist consisting of lift-off-resist (LOR 5A) and series photoresist (SPR 3012) and baked at 185 °C and 95 °C, respectively. The bilayer photoresist was then exposed using a Heidelburg maskless aligner (MLA 150) to define the island, and then developed using MF CD26 microposit followed by a deionized water rinse. The back-gate electrode of 20/50 nm TiN/Pt was deposited using reactive sputtering. The photoresist was removed using acetone and photoresist stripper (PRS 3000) and the substrate was then cleaned using 2-propanol (IPA) and deionized water. An atomic layer deposition process was then implemented to grow 50 nm Al_2O_3 across the entire substrate, including the island regions. To access the individual platinum back-gate electrodes, etch patterns were defined using the same bilayer photoresist (LOR 5A and SPR 3012). The bilayer photoresist was then exposed using the MLA 150 and developed using MF CD26 microposit. The 50 nm Al_2O_3 was subsequently dry etched using a BCl_3 reactive ion etch chemistry at 5 °C for 20 s, which was repeated four times to minimize heating in the substrate. Finally, the photoresist was removed to give access to the individual platinum electrodes.

Large-area monolayer MoS_2 film growth

Monolayer MoS_2 was deposited on epi-ready 2 inch *c*-sapphire substrate by metal–organic chemical vapour deposition (MOCVD). An inductively heated graphite susceptor equipped with wafer rotation in a cold-wall horizontal reactor was used to achieve uniform monolayer deposition as previously described[41]. Molybdenum hexacarbonyl ($Mo(CO)_6$) and hydrogen sulfide (H_2S) were used as precursors. $Mo(CO)_6$ maintained at 25 °C and 375 torr in a stainless-steel bubbler was used to deliver a nominal 2.0×10^{-2} sccm of the metal precursor for the growth, while 400 sccm of H_2S and 4,100 sccm of H_2 were used for the process. MoS_2 deposition was carried out at 900 °C and 50 torr in H_2 ambient, where monolayer growth was achieved in 15 min. The substrate was first heated to 900 °C in H_2 and maintained for 10 min before the growth was initiated. After growth, the substrate was cooled in H_2 and H_2S to 400 °C to inhibit decomposition of the MoS_2 films. More details can be found in our earlier work[15,42,43].

MoS_2 film transfer to local back-gate islands

To fabricate the MoS_2 field-effect transistors, the MOCVD-grown monolayer MoS_2 film was first transferred from the sapphire growth substrate to the SiO_2/p^{++}-Si substrate with local back-gate islands using a polymethyl-methacrylate (PMMA)-assisted wet transfer process. First, the MoS_2 on the sapphire substrate was spin-coated with PMMA and left to sit for 24 h to ensure good PMMA/MoS_2 adhesion. The corners of the spin-coated film were scratched using a razor blade and immersed inside a 2 M NaOH solution kept at 90 °C. Capillary action caused the NaOH to be preferentially drawn into the substrate/film interface due to the hydrophilic nature of sapphire and the hydrophobic nature of MoS_2 and PMMA, separating the PMMA/MoS_2 film from the sapphire substrate. The separated film was then fished from the NaOH solution using a clean glass slide and rinsed in three separate water baths for 15 min each before finally being transferred onto the application substrate. Subsequently, the substrate was baked at 50 °C and 70 °C for 10 min each to remove moisture and promote film adhesion, thus ensuring a pristine interface, before the PMMA was removed using acetone and the film was cleaned with IPA.

Fabrication of monolayer MoS_2 phototransistor

To define the channel regions for the MoS_2 phototransistors, the substrate was spin-coated with PMMA and baked at 180 °C for 90 s. The resist was then exposed via an electron beam (e-beam) and developed using a 1:1 mixture of 4-methyl-2-pentanone (MIBK) and IPA. The monolayer MoS_2 film was subsequently etched using a sulfur hexafluoride (SF_6) reactive ion etch chemistry at 5 °C for 30 s. Next, the sample was rinsed in acetone and IPA to remove the e-beam resist. To define the source and drain contacts, the sample was then spin coated with methyl methacrylate (MMA) followed by A3 PMMA. E-beam lithography was again used to pattern the source and drain contacts. The sample was then developed using a 1:1 mixture of MIBK/IPA for 60 s and pure IPA for 45 s. Next, 40 nm of nickel and 30 nm of gold were deposited using e-beam evaporation. Finally, a lift-off process was performed to remove the evaporated nickel/gold except from the source/drain patterns by immersing the sample in acetone for 30 min followed by IPA for another 30 min. Each island contained one MoS_2 field-effect transistor to allow for individual gate control.

Fabrication of MoS_2 phototransistor crossbar

To define the crossbar architecture connecting the source and drain of the phototransistors in a row, the sample was spin-coated with MMA and baked at 150 °C for 90 s before applying PMMA A3, which was baked 185 °C for 90 s. Both resists were spun at 4,000 r.p.m. for 45 s. E-beam lithography was used to pattern the crossbar connections, and development was again performed using a 1:1 mixture of MIBK and IPA for 60 s and pure IPA for 45 s. Next, 60 nm of nickel and 30 nm of gold were deposited using e-beam evaporation. Finally, lift-off of the evaporated material was performed by immersing the sample in acetone for 30 min and in IPA for 15 min.

TEM

HAADF-STEM was performed using an aberration-corrected ThermoFisher Titan^3 G2 60–300 with monochromator and X-field emission gun source at an accelerating voltage of 80 kV. The convergence semi-angle used for STEM imaging was 30.0 mrad and the collection angle range of the HAADF detector was 42–244 mrad. An SAED spot pattern was collected using a ThermoFisher Talos F200X transmission electron microscope at an accelerating voltage of 200 kV.

SHG

Polarization-resolved SHG microscopy was performed using a home-built instrument in which an 800 nm laser fundamental (Coherent, Vitara) was focused onto the sample with an aspheric lens (0.23 numerical aperture). Nonlinear emission was collected with a 100× oil-immersion objective (1.3 numerical aperture, Amscope) and isolated from the fundamental with a shortpass filter before imaging in a combined spectrograph/electron multiplication charge-coupled device (Andor, Shamrock 303i/ iXion Ultra). For the measurements shown in Fig. 2i,j, an analyser was placed at a fixed angle before the detector, and a half-wave plate inserted before the sample was rotated to vary the fundamental polarization. For these measurements, an analyser was placed at a fixed angle before the detector to collect the harmonic signal at a single polarization and a half-wave plate was inserted before the sample was rotated to vary the fundamental polarization. Each pixel of the resulting polarization data was fitted using equation (2).

$$y(\alpha) = \text{amplitude} \times (cos^2(3\theta - 2\alpha) + b) \quad (2)$$

Here, θ is the crystal orientation, α is the polarization of the fundamental and b is a factor indicative of the local disorder. For the measurements shown in Supplementary Information 1, the total harmonic signal (without an analyser in the detection path) was detected as a function of the fundamental polarization.

XPS

XPS experiments were performed using a Physical Electronics VersaProbe III instrument equipped with a monochromatic Al Kα X-ray source ($h\nu$ = 1,486.6 eV) and a concentric hemispherical analyser. Charge neutralization was performed using both low-energy electrons

(<5 eV) and argon ions. The binding energy axis was calibrated using sputter-cleaned copper (Cu $2p_{3/2}$ = 932.62 eV, Cu $3p_{3/2}$ = 75.1 eV) and gold foils (Au $4f_{7/2}$ = 83.96 eV)[44]. Spectra on the gold samples were charge referenced to Au^0 band in the Au 4*f* spectra at 84.0 eV. The MoS_2 spectra were charge referenced to sulfide band in the sulfur $2p_{3/2}$ spectra at 162.0 eV. Measurements were made at a takeoff angle of 45° with respect to the sample surface plane. This resulted in a typical sampling depth of 3–6 nm (95% of the signal originated from this depth or shallower). Quantification was done using instrumental relative sensitivity factors that account for the X-ray cross section and inelastic mean free path of the electrons. On homogeneous samples, major elements (>5 at%) tend to have standard deviations of <3% while minor elements can be notably higher. The analysis size was ~200 µm in diameter.

Raman and PL spectroscopy

The Raman and PL spectroscopy was performed on a Horiba LabRAM HR Evolution confocal Raman microscope with a 532 nm laser. The power was 40 mW filtered at 1% to 400 µW. The objective magnification was 500× with a numerical aperture of 0.9, and the grating had a spacing of 1,800 grooves per mm for Raman and 300 grooves per mm for PL.

AFM

AFM was used to study the surface morphology, domain size, coverage and thickness of the deposited layers. Scanasyst air probe AFM tips with a nominal tip radius of ~2 nm and a spring constant of 0.4 N m^{-1} were used for the measurements, and images were collected in peak-force tapping mode with a peak force of 500 pN and a scan speed of 2 Hz.

Electrical characterization

Electrical characterization of the fabricated devices was performed using a Lake Shore CRX-VF probe station under atmospheric conditions with a Keysight B1500A parameter analyser.

Reporting summary

Further information on research design is available in the Nature Research Reporting Summary linked to this article.

Data Availability

The datasets generated during and/or analysed during the current study are available from the corresponding author on reasonable request.

Code Availability

The codes used for plotting the data are available from the corresponding authors on reasonable request.

References

41. Xuan, Y. et al. Multi-scale modeling of gas-phase reactions in metal–organic chemical vapor deposition growth of WSe_2. *J. Cryst. Growth* https://doi.org/10.1016/j.jcrysgro.2019.125247 (2019).
42. Sebastian, A., Pendurthi, R., Choudhury, T. H., Redwing, J. M. & Das, S. Benchmarking monolayer MoS_2 and WS_2 field-effect transistors. *Nat. Commun.* **12**, 693 (2021).
43. Dodda, A. et al. Stochastic resonance in MoS_2 photodetector. *Nat. Commun.* **11**, 4406 (2020).
44. Seah, M. Summary of ISO/TC 201 standard: VII ISO 15472: 2001—surface chemical analysis—X-ray photoelectron spectrometers—calibration of energy scales. *Surf. Interface Anal.* **31**, 721–723 (2001).

Acknowledgements

The work of A.D., D.J., A.P., S.S.R. and S.D. was supported by Army Research Office (ARO) through contract number W911NF1920338 and the National Science Foundation (NSF) through CAREER Award under grant number ECCS-2042154. The work of N.T. and J.M.R. was supported by the NSF through the Pennsylvania State University 2D Crystal Consortium–Materials Innovation Platform (2DCCMIP) under NSF cooperative agreement DMR-1539916. The work of M.A.S., C.W.O. and K.L.K. was supported by the Air Force Office of Scientific Research grant number FA-9550-18-1-0347. The work of S.B. is supported by NSF CAREER DMR-1654107. The work of S.P.S. and D.E.W. was supported by the Department of Defense, Defense Threat Reduction Agency (DTRA) as part of the Interaction Ionizing Radiation with Matter University Research Alliance (IIRM-URA) under contract number HDTRA1-20-2-0002. The content of the information does not necessarily reflect the position or the policy of the federal government, and no official endorsement should be inferred.

Author contributions

S.D., A.D. and D.J. conceived the idea and designed the experiments. A.D., D.J., A.P., S.S.R. and S.D. performed the experiments, analysed the data, discussed the results and agreed on their implications. N.T. grew MOCVD MoS_2 under the supervision of J.M.R. S.B. helped in the TEM sample preparation. S.P.S. performed the TEM characterization under the supervision of D.E.W. M.A.S. and C.W.O. performed the SHG measurements and simulations under the supervision of K.L.K. J.R.S. helped with the XPS measurements and analysis. All authors contributed to the preparation of the manuscript.

Competing interests

The authors declare no competing interests.

Additional information

Extended data is available for this paper at https://doi.org/10.1038/s41563-022-01398-9.

Supplementary information The online version contains supplementary material available at https://doi.org/10.1038/s41563-022-01398-9.

Correspondence and requests for materials should be addressed to Saptarshi Das.

Peer review information *Nature Materials* thanks Sunkook Kim, Dmitry Polyushkin and the other, anonymous, reviewer(s) for their contribution to the peer review of this work.

https://doi.org/10.1038/s41563-022-01398-9

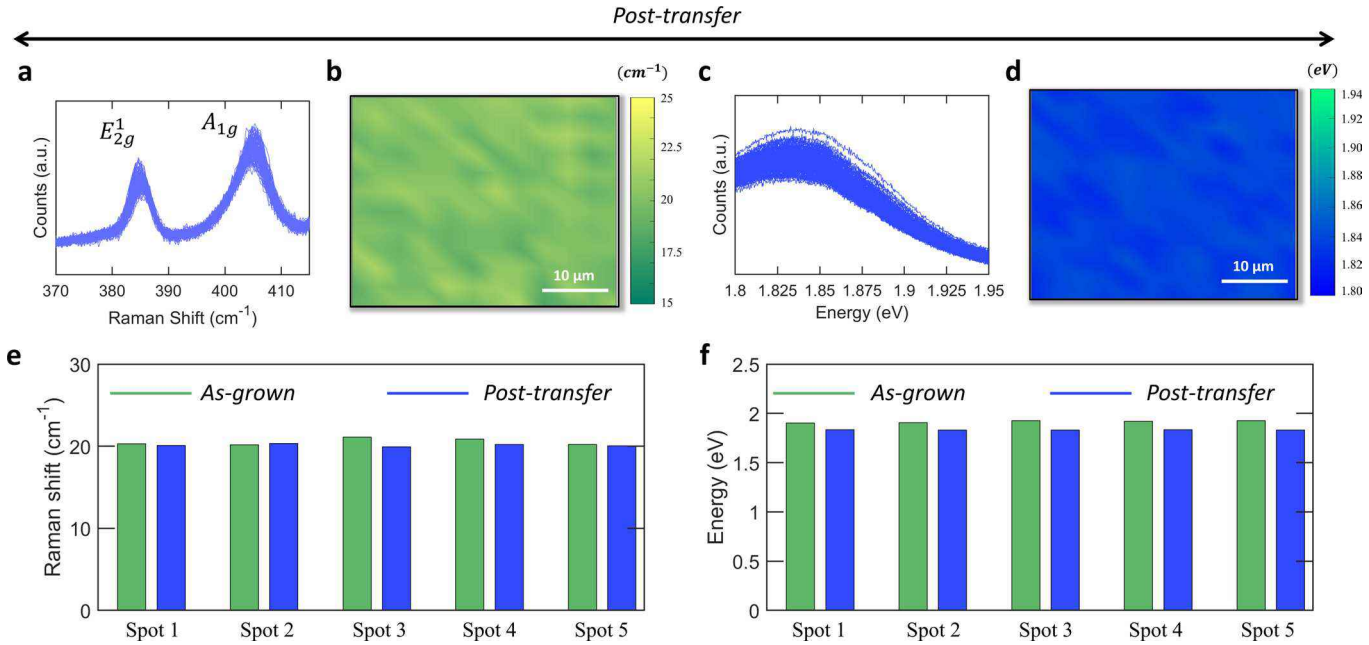

Extended Data Fig. 1 | Raman spectroscopy of monolayer MoS_2. a, Raman spectra, and **b**, corresponding spatial colormap of peak separation between the two Raman active modes, E^1_{2g} and A_{1g}, **c**, PL spectra, and **d**, corresponding spatial colormap of PL peak position measured over a 40 μm × 40 μm area for post-transfer MoS_2 film. The mean Raman peak separation was found to be ~20 cm^{-1} with a standard deviation of ~0.72 cm^{-1} and the mean PL peak position was found to be at ~1.83 eV with a standard deviation of ~0.005 eV for the post-transfer film, respectively. Bar plots for **e**, the mean peak separation between E^1_{2g} and A_{1g} Raman modes and **f**, mean PL peak position along with their corresponding standard deviation values for as-grown and post-transfer films obtained over 40 μm × 40 μm areas for 5 different locations.

https://doi.org/10.1038/s41563-022-01398-9

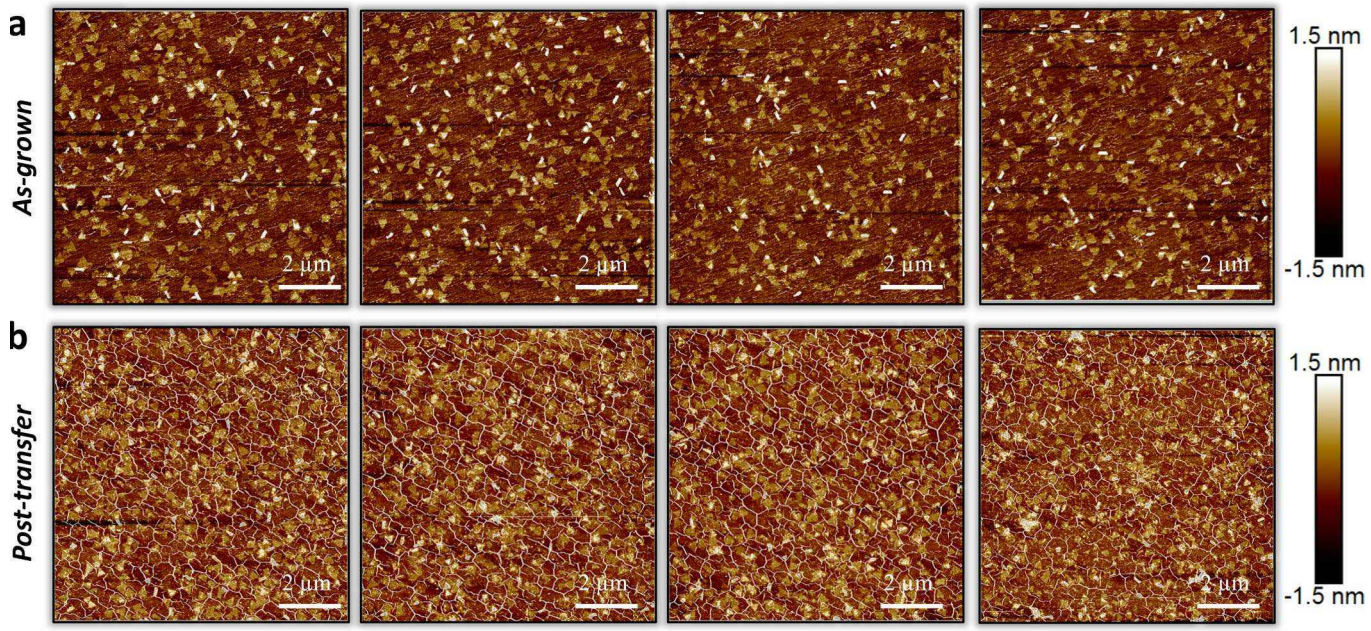

Extended Data Fig. 2 | Atomic force microscopy (AFM) of monolayer MoS_2. AFM images were taken at 4 different locations for **a**, as-grown and **b**, post-transfer MoS_2 films. Although the thickness of both films was ~1 nm, we do observe polymer residues concentrating near the edges of bilayer islands and/or grain boundaries in the transferred film. This is typical of polymer-assisted transfer processes.

https://doi.org/10.1038/s41563-022-01398-9

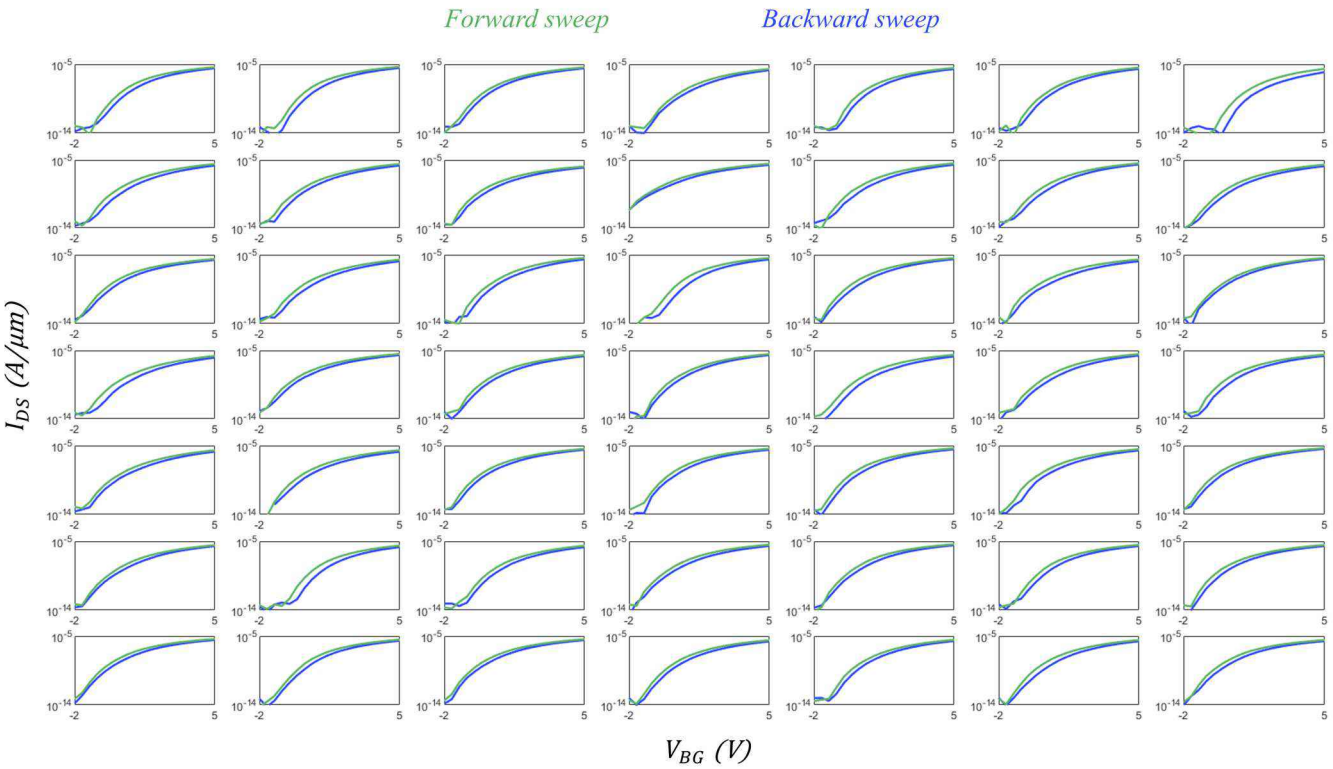

Extended Data Fig. 3 | Hysteresis in the transfer characteristics of 2D APS. Hysteresis in the transfer characteristics of 49 2D APS.

https://doi.org/10.1038/s41563-022-01398-9

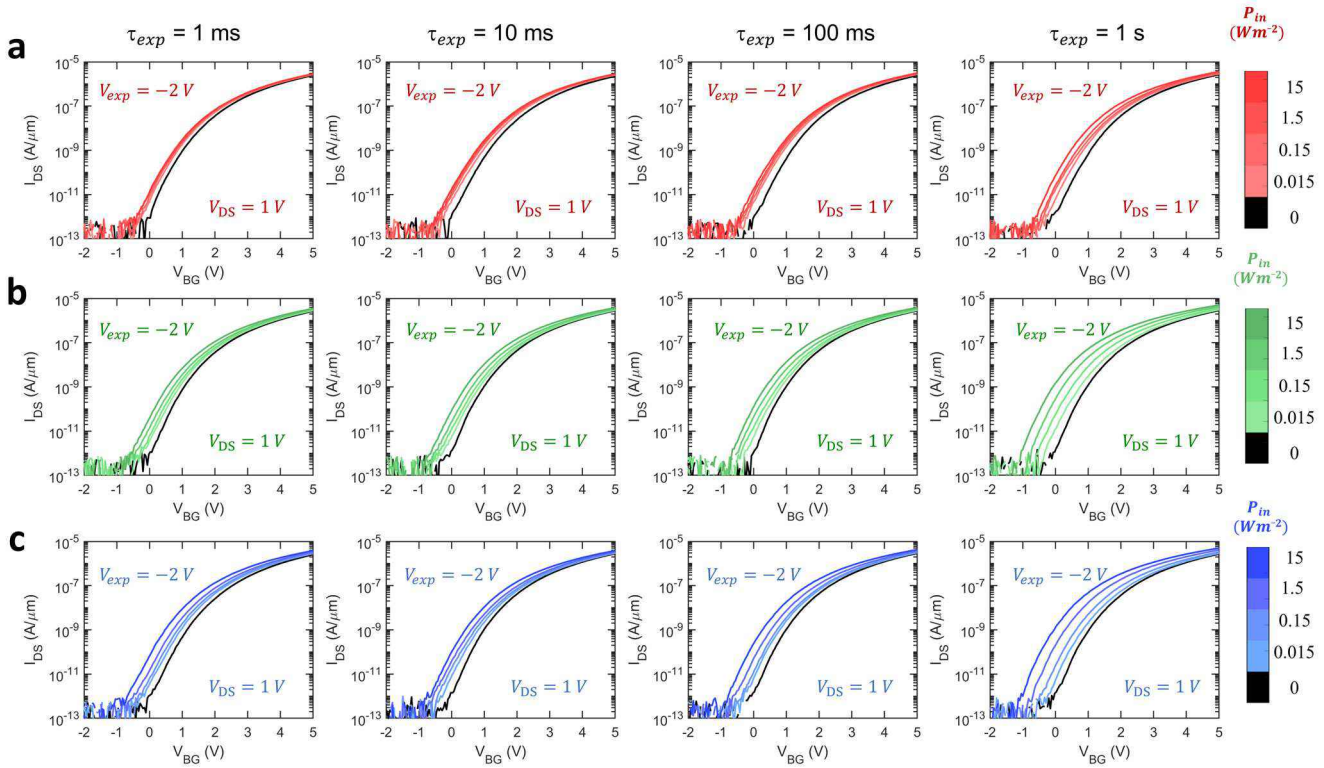

Extended Data Fig. 4 | Post-illumination transfer characteristics of the 2D APS when exposed to different illumination intensities (P_{in}) for different duration (τ_{exp}). Post-illumination transfer characteristics of the 2D APS when exposed to different P_{in} for different τ_{exp} periods for **a**, red, **b**, green, and **c**, blue illuminations, respectively. All illuminations were done at $V_{exp} = -2$ V.

https://doi.org/10.1038/s41563-022-01398-9

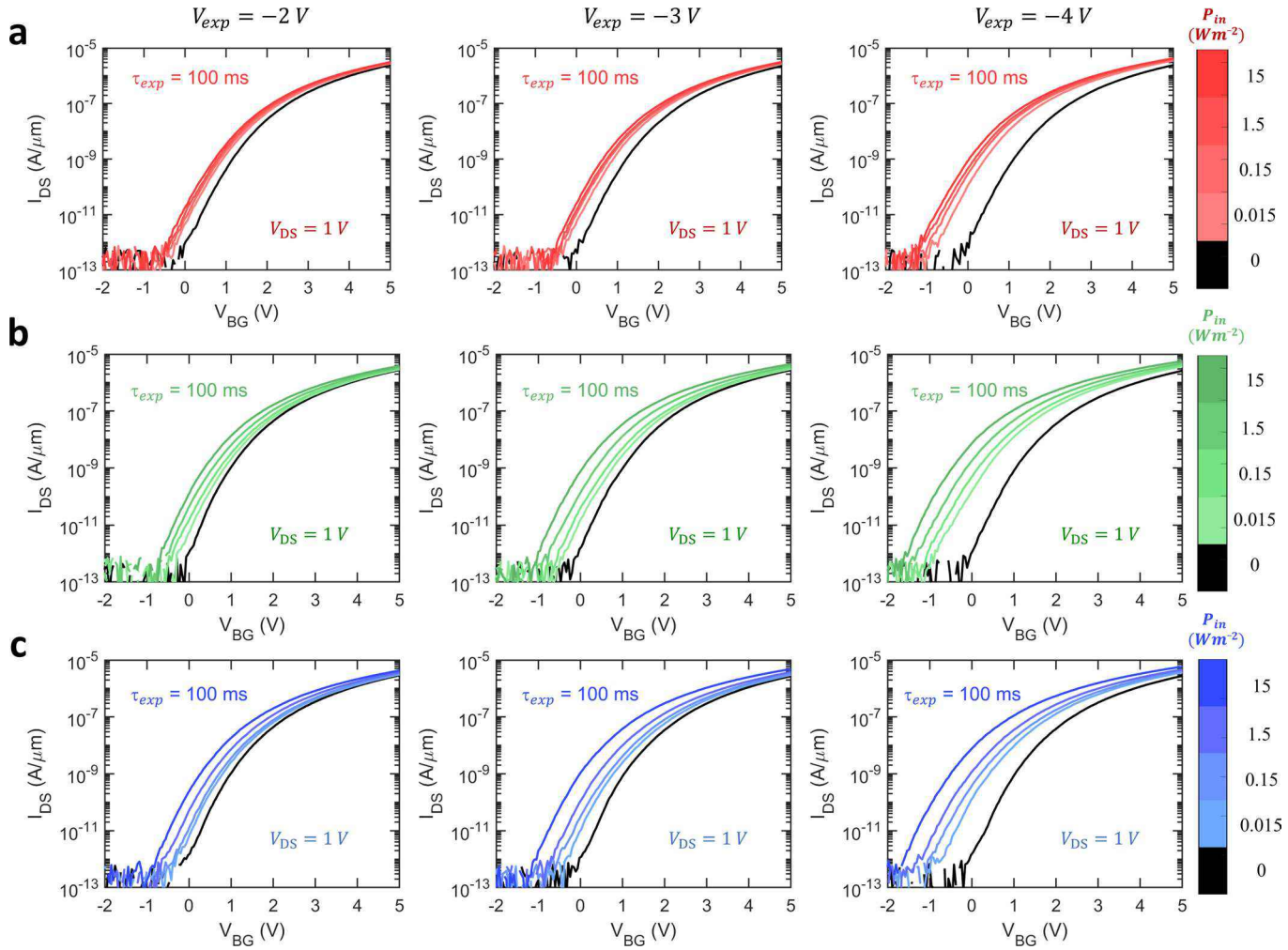

Extended Data Fig. 5 | Post-illumination transfer characteristics of the 2D APS when exposed to different illumination intensities (P_{in}) at different gate bias (V_{exp}). Post-illumination transfer characteristics of the 2D APS when exposed to different P_{in} for different V_{exp} values for **a**, red, **b**, green, and **c**, blue illuminations, respectively. All illuminations were done for τ_{exp} = 100 ms.

https://doi.org/10.1038/s41563-022-01398-9

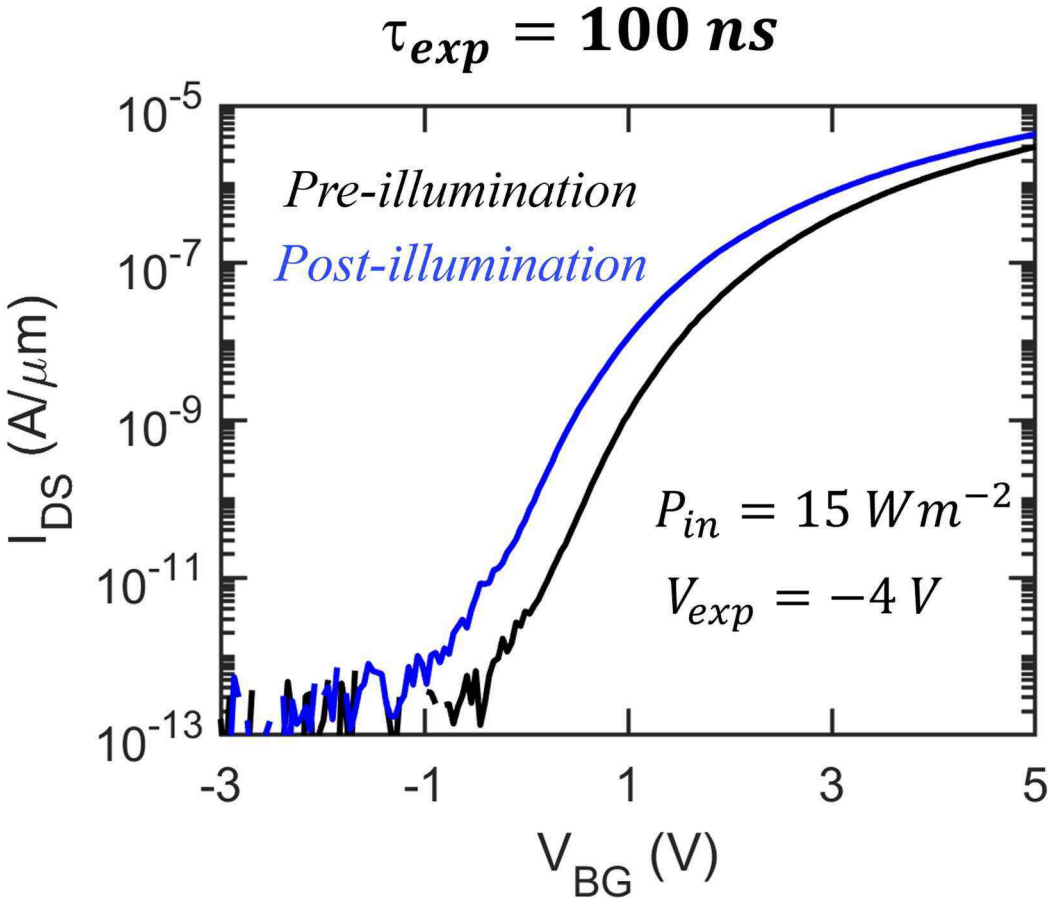

Extended Data Fig. 6 | Pre- and post-illumination transfer characteristics of a MoS_2 phototransistor. Pre- and post-illumination transfer characteristics of a representative MoS_2 phototransistor after being exposed to blue illumination with $P_{in} = 15\ Wm^{-2}$ at $V_{exp} = -4$ V for $\tau_{exp} = 100$ ns. Clearly, we observe a change in the post-illumination transfer characteristics, indicating that the charge trapping in the MoS_2 phototransistor can occur as fast as 100 ns.

nature portfolio

Corresponding author(s): Saptarshi Das

Last updated by author(s): Oct 3, 2022

Reporting Summary

Nature Portfolio wishes to improve the reproducibility of the work that we publish. This form provides structure for consistency and transparency in reporting. For further information on Nature Portfolio policies, see our Editorial Policies and the Editorial Policy Checklist.

Statistics

For all statistical analyses, confirm that the following items are present in the figure legend, table legend, main text, or Methods section.

n/a	Confirmed
☒	☐ The exact sample size (*n*) for each experimental group/condition, given as a discrete number and unit of measurement
☒	☐ A statement on whether measurements were taken from distinct samples or whether the same sample was measured repeatedly
☒	☐ The statistical test(s) used AND whether they are one- or two-sided *Only common tests should be described solely by name; describe more complex techniques in the Methods section.*
☒	☐ A description of all covariates tested
☒	☐ A description of any assumptions or corrections, such as tests of normality and adjustment for multiple comparisons
☒	☐ A full description of the statistical parameters including central tendency (e.g. means) or other basic estimates (e.g. regression coefficient) AND variation (e.g. standard deviation) or associated estimates of uncertainty (e.g. confidence intervals)
☒	☐ For null hypothesis testing, the test statistic (e.g. *F*, *t*, *r*) with confidence intervals, effect sizes, degrees of freedom and *P* value noted *Give P values as exact values whenever suitable.*
☒	☐ For Bayesian analysis, information on the choice of priors and Markov chain Monte Carlo settings
☒	☐ For hierarchical and complex designs, identification of the appropriate level for tests and full reporting of outcomes
☒	☐ Estimates of effect sizes (e.g. Cohen's *d*, Pearson's *r*), indicating how they were calculated

Our web collection on statistics for biologists contains articles on many of the points above.

Software and code

Policy information about availability of computer code

Data collection	N/A
Data analysis	N/A

For manuscripts utilizing custom algorithms or software that are central to the research but not yet described in published literature, software must be made available to editors and reviewers. We strongly encourage code deposition in a community repository (e.g. GitHub). See the Nature Portfolio guidelines for submitting code & software for further information.

Data

Policy information about availability of data

All manuscripts must include a data availability statement. This statement should provide the following information, where applicable:

- Accession codes, unique identifiers, or web links for publicly available datasets
- A description of any restrictions on data availability
- For clinical datasets or third party data, please ensure that the statement adheres to our policy

N/A

Field-specific reporting

Please select the one below that is the best fit for your research. If you are not sure, read the appropriate sections before making your selection.

☒ Life sciences ☐ Behavioural & social sciences ☐ Ecological, evolutionary & environmental sciences

For a reference copy of the document with all sections, see nature.com/documents/nr-reporting-summary-flat.pdf

Life sciences study design

All studies must disclose on these points even when the disclosure is negative.

Sample size	N/A
Data exclusions	N/A
Replication	N/A
Randomization	N/A
Blinding	N/A

Reporting for specific materials, systems and methods

We require information from authors about some types of materials, experimental systems and methods used in many studies. Here, indicate whether each material, system or method listed is relevant to your study. If you are not sure if a list item applies to your research, read the appropriate section before selecting a response.

Materials & experimental systems

n/a	Involved in the study
☒	☐ Antibodies
☒	☐ Eukaryotic cell lines
☒	☐ Palaeontology and archaeology
☒	☐ Animals and other organisms
☒	☐ Human research participants
☒	☐ Clinical data
☒	☐ Dual use research of concern

Methods

n/a	Involved in the study
☒	☐ ChIP-seq
☒	☐ Flow cytometry
☒	☐ MRI-based neuroimaging